Enhanced Photo-Fenton Degradation of Antibiotics through Internal Electric Field Formation at the Interface of Mixed-Phase FeS_2

Hongyan Liu [1,2], Yunhang Shao [1,2], Shuai Dou [1,2], and Chengsi Pan [1,2,*]

[1] Key Laboratory of Synthetic and Biological Colloids, Ministry of Education, School of Chemical and Material Engineering, Jiangnan University, Wuxi 214122, China
[2] International Joint Research Center for Photoresponsive Molecules and Materials, Jiangnan University, Wuxi 214122, China
* Correspondence: cspan@jiangnan.edu.cn

S1. Experimental Section

S1.1 Calculation of the Contribution of Active Species

The contribution of each ROS species is calculated by Equations (1)–(3) and the first-order Reaction rate constant:

$$R_{1_{O_2}} = \frac{K_{1_{O_2}}}{K} = \frac{K - K_{L-his}}{K} \quad (1)$$

$$R_{\cdot OH} = \frac{K_{\cdot OH}}{K} = \frac{K - K_{IPA}}{K} \quad (2)$$

$$R_{\cdot O_2^-} = \frac{K_{\cdot O_2^-}}{K} = \frac{K - K_{PBQ}}{K} \quad (3)$$

where R is the contribution of reaction species without quenching agent to the Reaction rate constant K of the reaction, K_i is the Reaction rate constant of the first order kinetic reaction of $^1O_2$, $\cdot O_2^-$, $\cdot OH$ in the presence of *L-His*, *BQ*, and *IPA*.

S1.2 DFT calculation

The electronic structural properties of the surface of P-FeS_2 and M-FeS_2 are calculated using the CASTEP package in Material Studio [1]. The surface is geometrically optimized to relax the surface. For geometrical optimization, a (2 × 2) mesh and the (111) planes on P-FeS_2 and (110) planes on M-FeS_2 with a fractional thickness of 0.5 including 2 Fe layers with a 15 Å vacuum gap are employed as the model surface. The ultrasoft pseudopotential is used for DFT calculations, and the cut-off energy is set to 380 eV. The Brillouin zone is integrated using a (2 × 2 × 2) k-points mesh. The exchange correlation energy is determined by generalized gradient approximation (GGA) and PBE function. The convergence criteria for energy, force, stress, and displacement are set as 5×10^{-5} eV/atom, 0.1 eV/Å, 0.2 GPa, and 0.005 Å, respectively.

The adsorption energy is calculated based on the optimized (111) surface of P-FeS_2 and (110) surface of M-FeS_2. The adsorption energies (E_{ads}) of the adsorbed H_2O_2 and H_2O on the given exposed FeS_2 surface are calculated by the following equation:

$$E_{ad=} E_{ads/sub} - (E_{ads} + E_{sub}) \quad (4)$$

where E_{ads}, E_{sub} and $E_{ads/sub}$ represent the total energy of the free adsorbate (H_2O or H_2O_2), the relaxed P-FeS_2 (111) and M-FeS_2 (110) surface, and the relaxed surface covered with the adsorbate, respectively. According to the formula, more negative adsorption energy means stronger interaction between the substrate and the adsorbate.

S2. Figures and Tables

Table S1. The crystal phase ratio of P/M-FeS_2 and M/P-FeS_2.

Mass Weight [a]/wt %	P-FeS_2	M-FeS_2
P/M-FeS_2	63.9%	36.1%
M/P-FeS_2	32.3%	67.7%

[a] The weight percentage of P-FeS_2 and M-FeS_2 in P/M-FeS_2 and M/P-FeS_2 is obtained by whole pattern fitting in XRD.

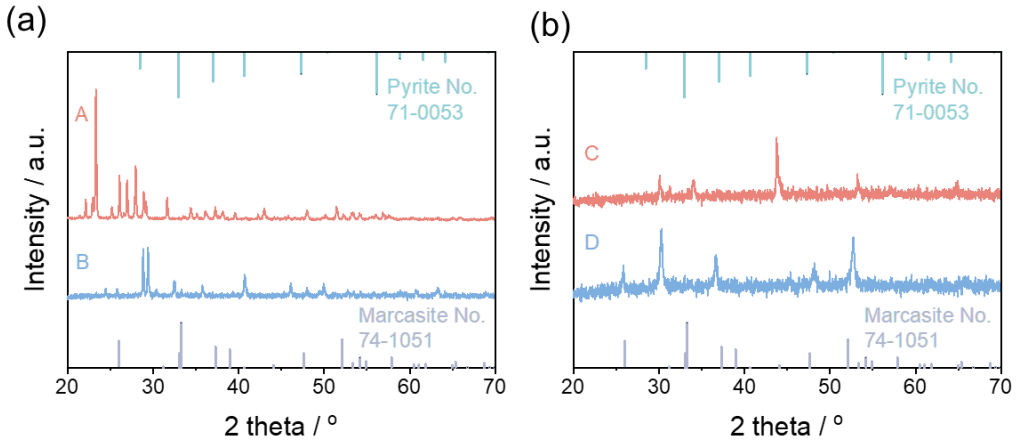

Figure S1. (**a**) P/M-FeS_2 synthesized from different iron sources. (**b**) P/M-FeS_2 synthesized from different sulfur sources.

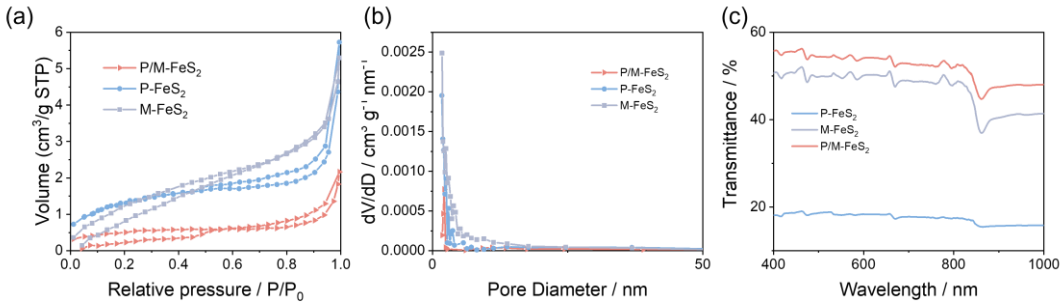

Figure S2. (**a**) N_2 adsorption/desorption isotherms (up) at 196°C for P-FeS_2, M-$FeS_2$and P/M-FeS_2 and (**b**) Pore size distribution (down) on P-FeS_2, M-$FeS_2$and P/M-FeS_2. (**c**) UV-Vis DRS spectra of P-FeS_2, M-$FeS_2$and P/M-FeS_2.

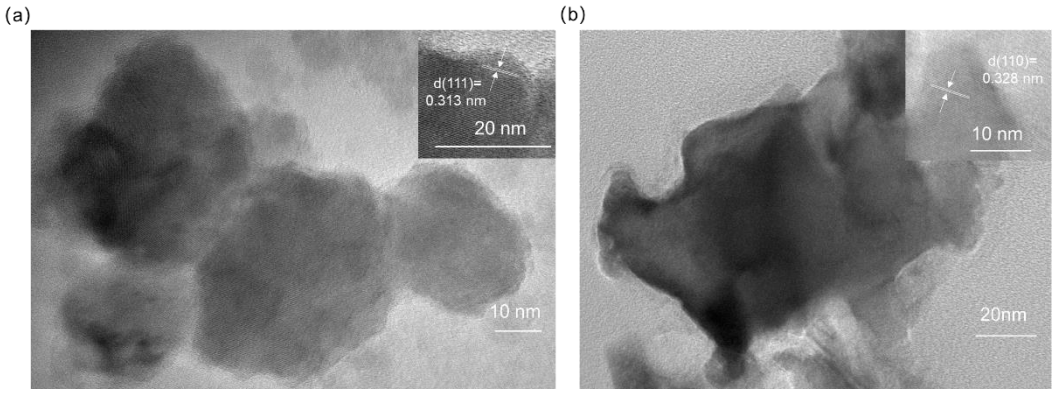

Figure S3. TEM images of (**a**) P-FeS_2 and (**b**) M-FeS_2. Inset is the HRTEM image for the concurrent phase.

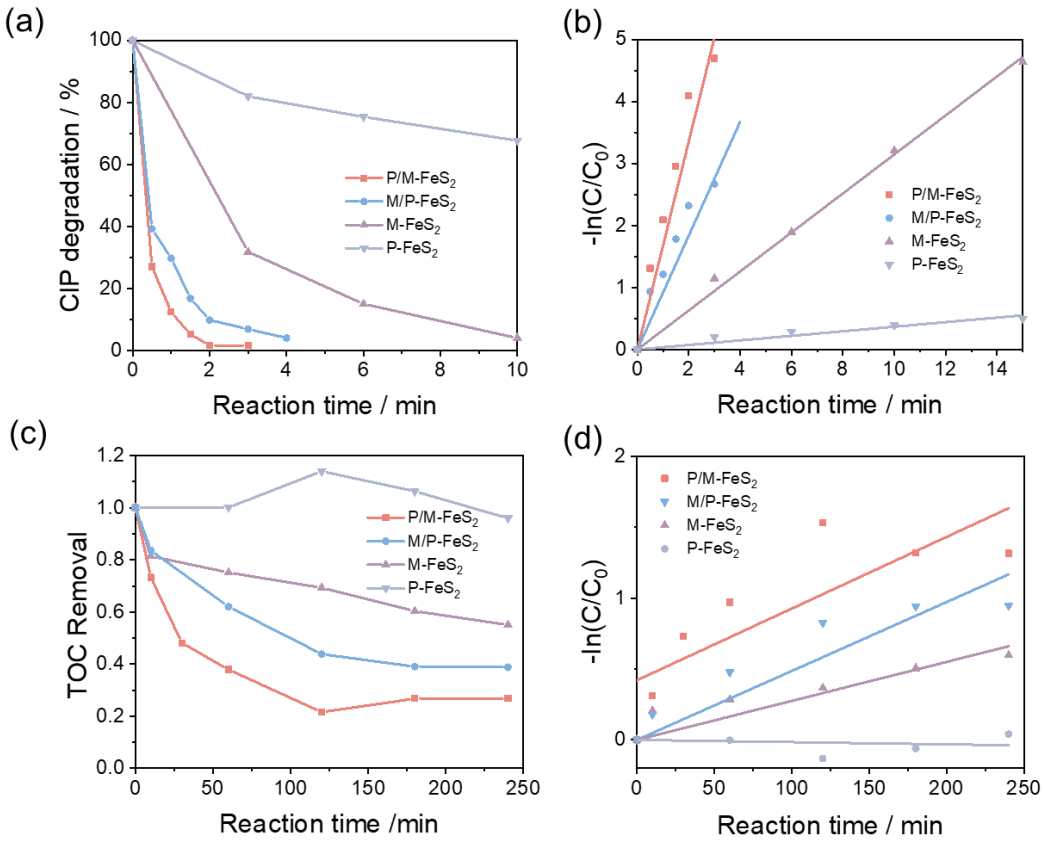

Figure S4. (**a**) Degradation curves of CIP with various crystal-phased FeS_2 catalysts. (**b**) Degradation rate constants of photo-Fenton degradation with various phased FeS_2 catalysts. (**c**) The TOC removal with various crystal-phased FeS_2 catalysts. (**b**) TOC removal rate constants with various phased FeS_2 catalysts.

Table S2. Comparison of photo-Fenton CIP degradation performance of P/M-FeS_2 with typical reported iron-based catalysts.

No.	Catalyst	Photo-Fenton performance	Ref.
1	P/M-FeS_2	50 ppm CIP, cat. 0.2 g/L, K = 1.42 min^{-1}, Xe lamp, Full-spectrum	This work
2	$LaFeO_3$/Diatomite	20 ppm CIP, cat. 0.3 g/L, K = 0.0187 min^{-1}, Xe lamp, Full-spectrum	2
3	g–C_3N_4/$NiCo_2O_4$/ $Zn_{0.3}Fe_{2.7}O_4$	50 ppm CIP, cat. 0.05 g/L, K = 0.0085 min^{-1}, 500 W tungsten lamp, λ > 400 nm	3
4	Fe-TCPP	14.5 ppm CIP, cat. 0.01 g /L, K = 0.0436 min^{-1}, Xe lamp, λ > 400 nm	4
5	ZrO_2@Fe_3O_4/WPC	20 ppm CIP, cat. 0.15 g/L, K = 0.032 min^{-1}, UV lamp, 185 nm < λ < 254 nm	5
6	m-PyC/FeOCl	10 ppm CIP, cat. 1 g/L, K = 0.1163 min^{-1}, Xe lamp, 700 nm > λ＞400 nm	6
7	α-(Fe, Cu)OOH/RGO	30 ppm CIP, cat. 0.4 g/L, 500 W tungsten halogen lamp, K = 0.0056 min^{-1}, 420 nm < λ <800 nm	7
8	Fe-MOF@BiOBr/M-CN	10 ppm CIP, cat. 0.63 g/L, K = 0.01645 min^{-1}, Xe lamp, λ > 420 nm	8
9	$BiVO_4$/NH_2-MIL-53(Fe)	10 ppm CIP, cat. 0.2 g/L, K = 0.0108 min^{-1}, Xe lamp, λ > 420 nm	9
10	Fe-HQLC/TiO_2	50 ppm CIP, cat. 1 g/L, K = 0.187 min^{-1}, Xe lamp, λ > 420 nm	10
11	Fe/N-CQDs/MCN1	15 ppm CIP, cat.0.5 g/L, K = 0.009 min^{-1}, Xe lamp, λ > 420 nm	11
12	$ZnFe_2O_4$/Fe_2O_3	10 ppm CIP, cat. 0.5 g/L, K = 0.0054 min^{-1}, Xe lamp, AM 1.5G	12
13	g-C_3N_4/Fe_3O_4@Fe -MIL−100	200 ppm CIP, cat. 0.67 g/L, K = 0.0656 min^{-1}, Xe lamp, λ＞ 420 nm	13

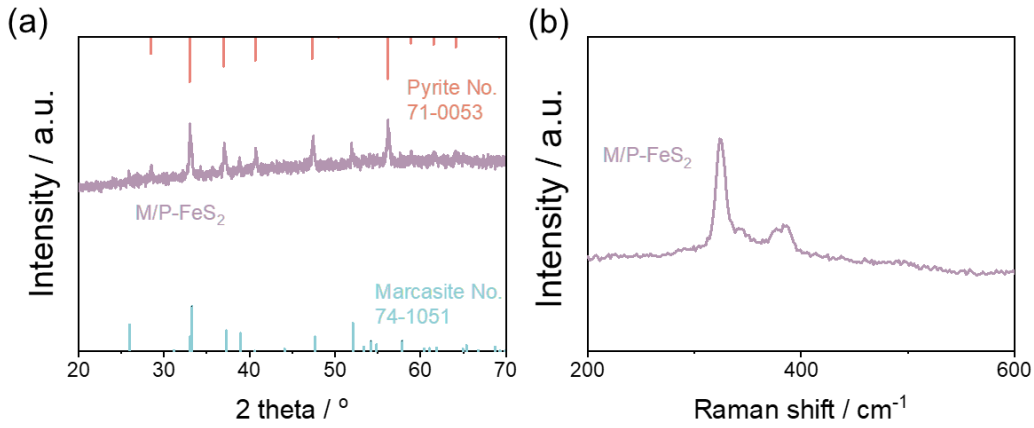

Figure S5. XRD (**a**) and Raman (**b**) of the prepared of M/P-FeS_2.

Table S3. The initial rate constant $k_{alachlor}$ (min^{-1}), BET surface area ($m^2 \cdot g^{-1}$), and the normalized initial rate constant with BET surface areas $k_{alachlor, surf}$ ($g \cdot min^{-1} \cdot m^{-2}$) of the samples.

Sample	$k_{alachlor}$ (min^{-1})	BET Surface Area ($m^2 \cdot g^{-1}$)	$k_{alachlor, surf}$ ($g \cdot min^{-1} \cdot m^{-2}$)
P-FeS_2	0.04	5.059	0.007
M-FeS_2	0.31	5.215	0.059
P/M-FeS_2	1.67	1.853	0.901

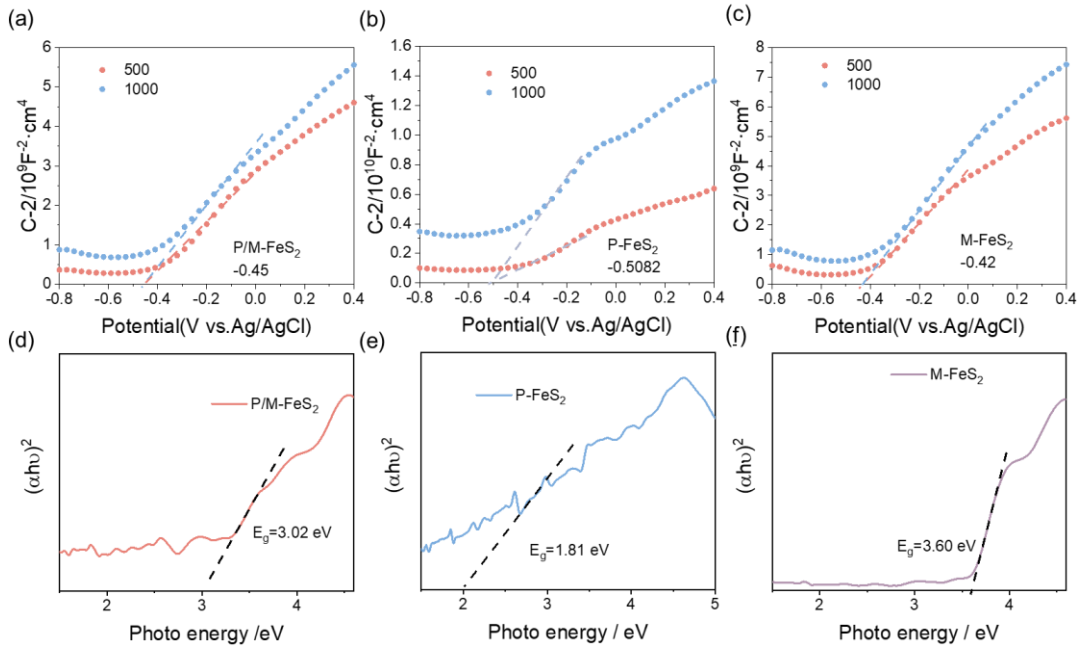

Figure S6. The Mott-Schottky plots and Tauc plots of the prepared FeS_2: (**a**,**d**) P/M-FeS_2; (**b**,**e**) P-FeS_2; (**c**,**f**) M-FeS_2.

The slope of the MS curves of the three types of FeS_2 are positive, which indicates that the three types of FeS_2 are n-type semiconductors. The flat-band potential (E_{fb}) of P/M-FeS_2, P-FeS_2 and M-FeS_2 obtained from the x intercepts of the linear region in MS plots (Fig. S6) were found to be -0.45, -0.51 and -0.42 V (vs. Ag/AgCl), namely -0.30, -0.21, 0.00 V (vs. NHE), respectively. The band edge positions of the three kinds of FeS_2 can be calculated using the following equation:

$$E_{CB}(V\ vs.\ NHE) = E_{fb}\left(V\ vs.\frac{Ag}{AgCl}\right) + 0.21 - X \cdots\cdots Eq.s1$$

$$E_{VB}=E_{CB}+E_g \cdots\cdots Eq\cdots s4$$

Where E_{VB} and E_{CB} stand for the valence band edge potential and conduction band edge potential, respectively; $E_{Ag/AgCl}$=0.210V vs. NHE; X is the voltage difference between the conduction band value and the flat potential value, generally 0.1-0.2 eV (the conduction bands of n-type semiconductors are normally 0.1-0.2 eV deeper than the flat-band potential), which is set as 0.1 eV in this work. the E_{CB} of P/M-FeS_2, P-$FeS_2$and M-FeS_2 are -0.34, -0.40 and -0.31 V (vs. NHE), respectively; E_g obtained by Tauc plots. (Fig. S6) the E_{VB} are 2.68, 1.41 and 3.29 V (vs. NHE), respectively. The results show that E_{CB} of P/M-FeS_2, P-$FeS_2$and M-FeS_2 are -0.34, -0.40 and -0.31 V (vs. NHE), respectively; the E_{VB} are 2.68, 1.41 and 3.29 V (vs. NHE), respectively.

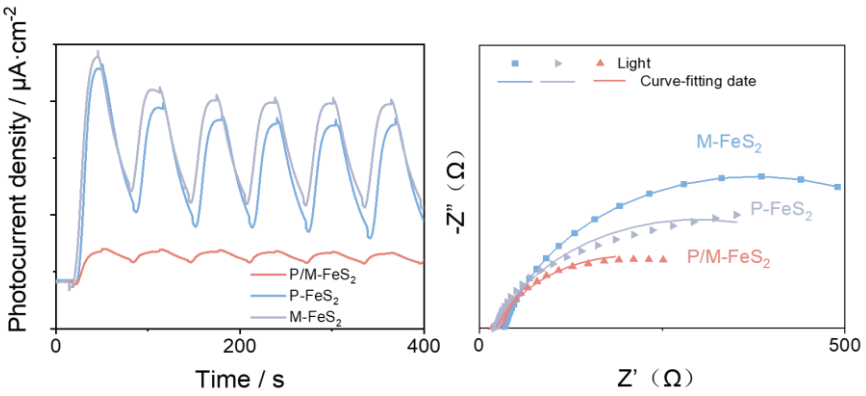

Figure S7. Transient photocurrent and EIS spectra of P/M-FeS_2, P-FeS_2 and M-FeS_2.

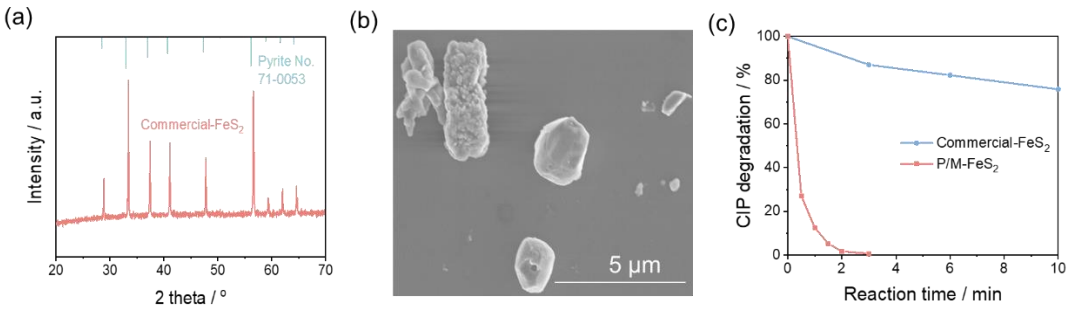

Figure S8. (**a**) XRD and (**b**) SEM of the Commercially purchased natural FeS_2. (**c**) Photo-Fenton Degradation of CIP with Commercial-FeS_2, and P/M-FeS_2.

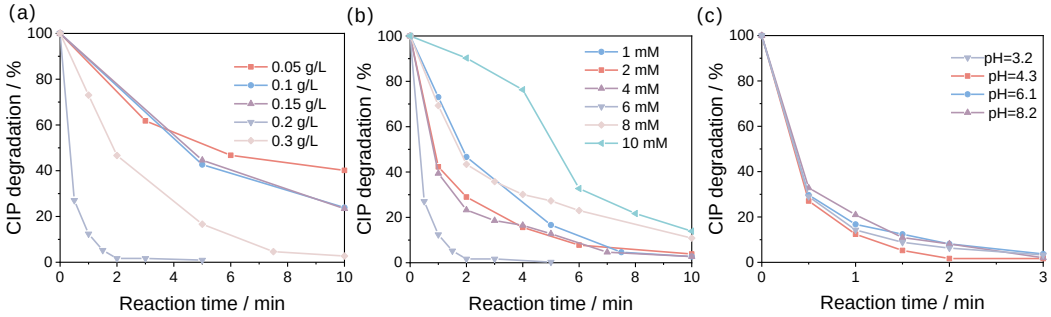

Figure S9. Fenton degradation of CIP with different dosages of P/M-FeS_2 catalyst (**a**), H_2O_2 (**b**), and different initial pH (**c**).

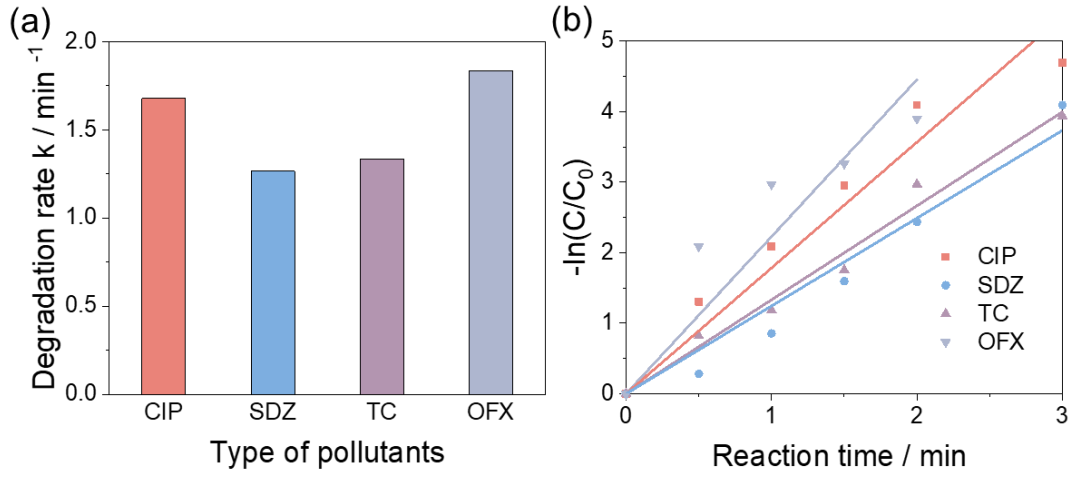

Figure S10. (**a**) Degradation rate constants for different pollutants in the P/M-FeS_2 photo-Fenton system. (**b**) Linear fitting of degradation curves with the concurrent pollutants.

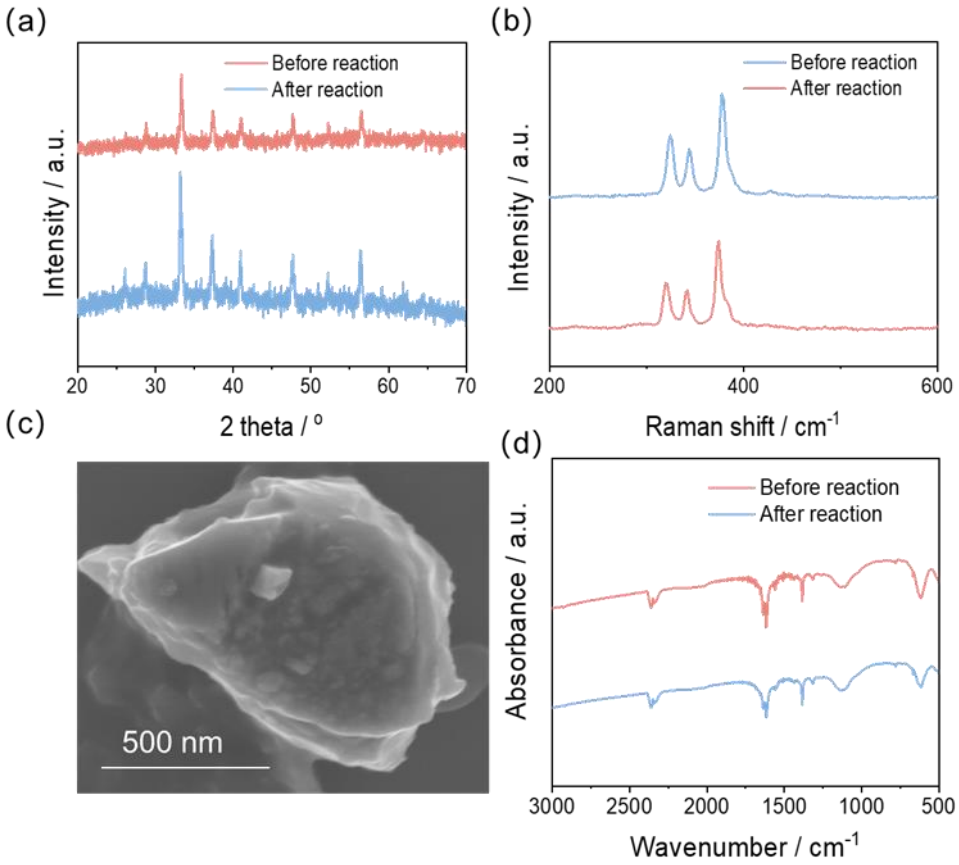

Figure S11. XRD (**a**), Raman (**b**), SEM (**c**) and FTIR (**d**) of P/M-FeS_2 before and after the reaction.

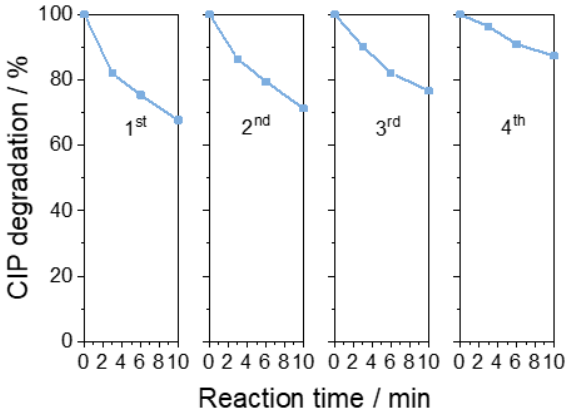

Figure S12. CIP degradation for 4 cycles with P-FeS_2.

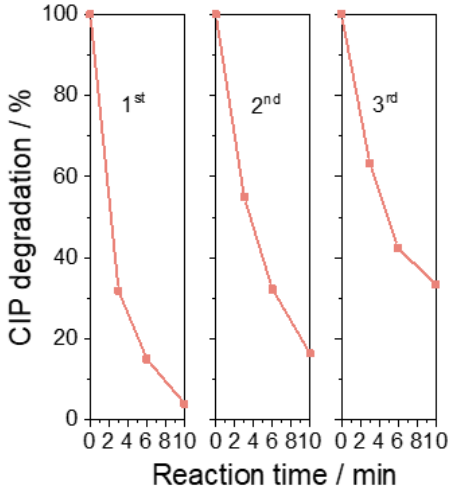

Figure S13. CIP degradation for 3 cycles with M-FeS_2.

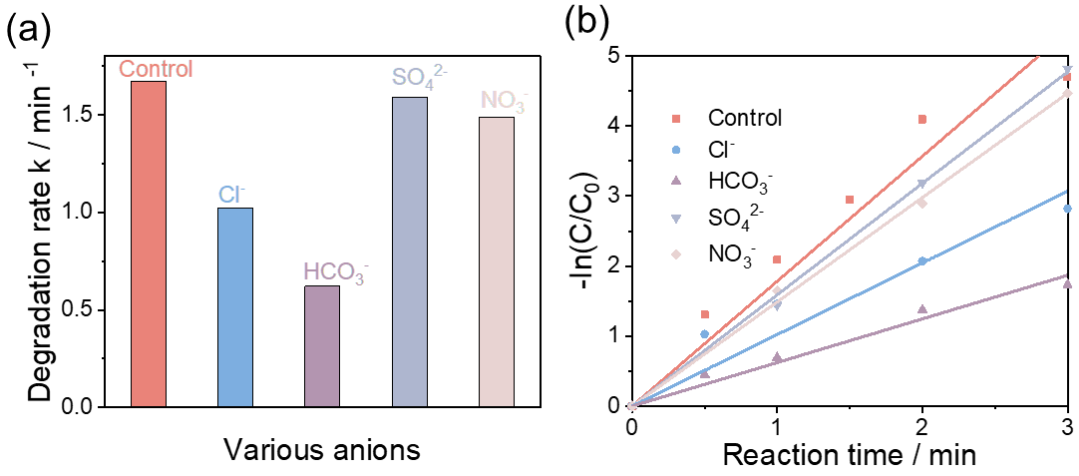

Figure S14. k values for the CIP degradation in the P/M-FeS_2 photo-Fenton system with the addition of 5 mM different anions (**a**) and linear fitting of the concurrent degradation curves (**b**).

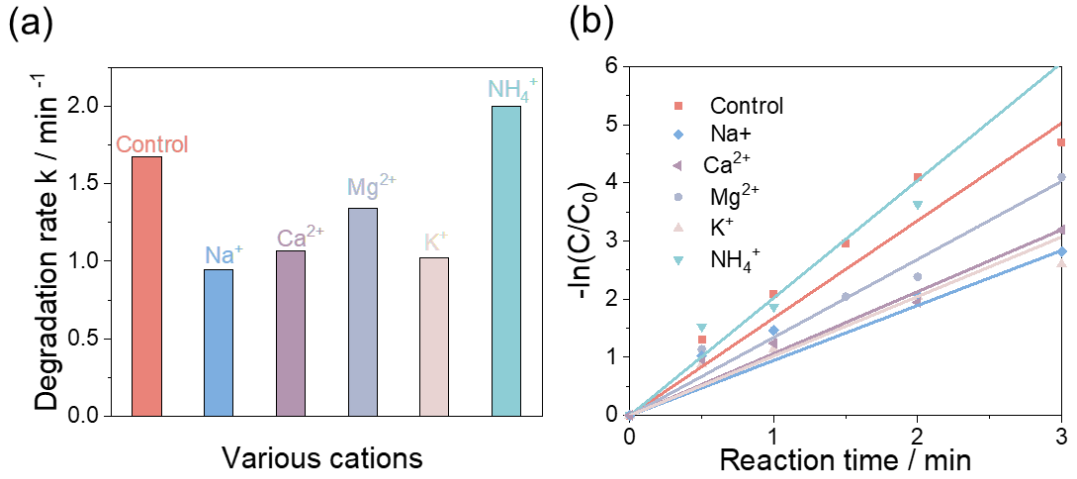

Figure S15. k values for the CIP degradation in the P/M-FeS_2 photo-Fenton system with the addition of 5 mM different cations (**a**) and linear fitting of the concurrent degradation curves (**b**).

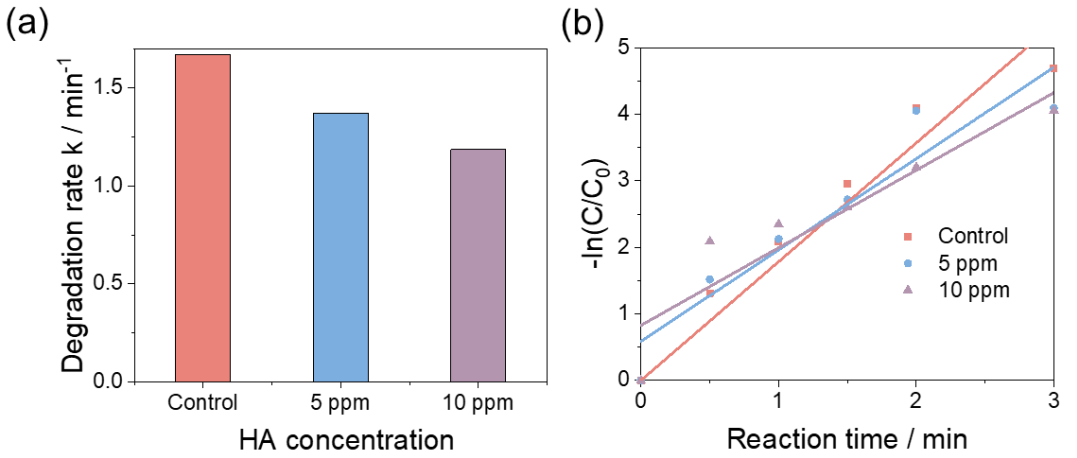

Figure S16. k values for the CIP degradation in the P/M-FeS_2 photo-Fenton system with the addition of different concentrations of HA (**a**) and linear fitting of the concurrent degradation curves (**b**).

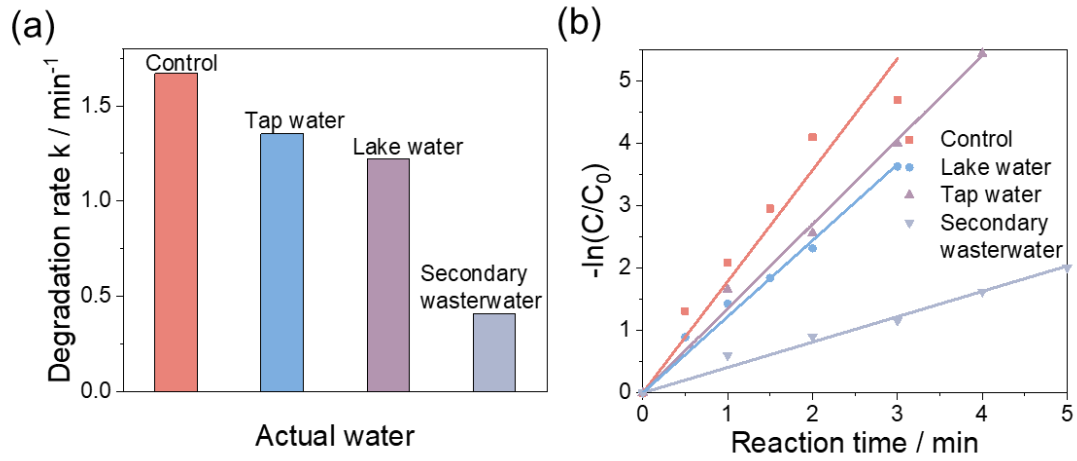

Figure S17. k values for the CIP degradation in the P/M-FeS_2 photo-Fenton system with the different sources of water (**a**) and linear fitting of the concurrent degradation curves (**b**).

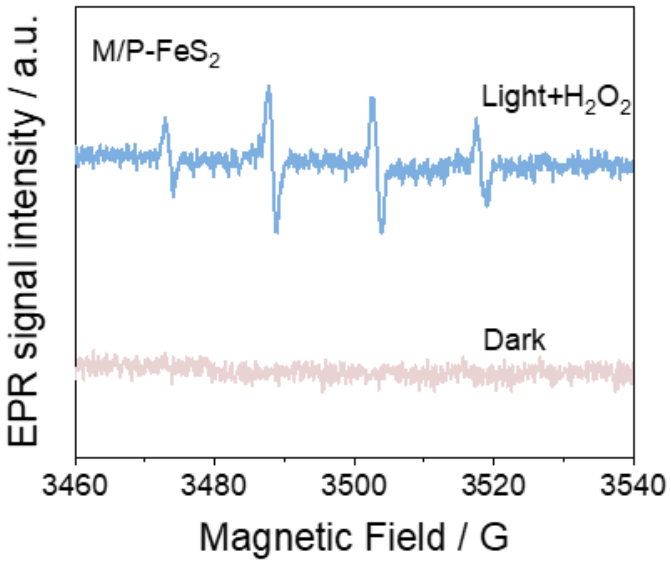

Figure S18. EPR signals of the M/P-FeS_2 in dark and with light irradiation and H_2O_2 addition. 5,5-Dimethyl−1-pyrroline-N-oxide (DMPO) as the spin-trapping reagent of •OH.

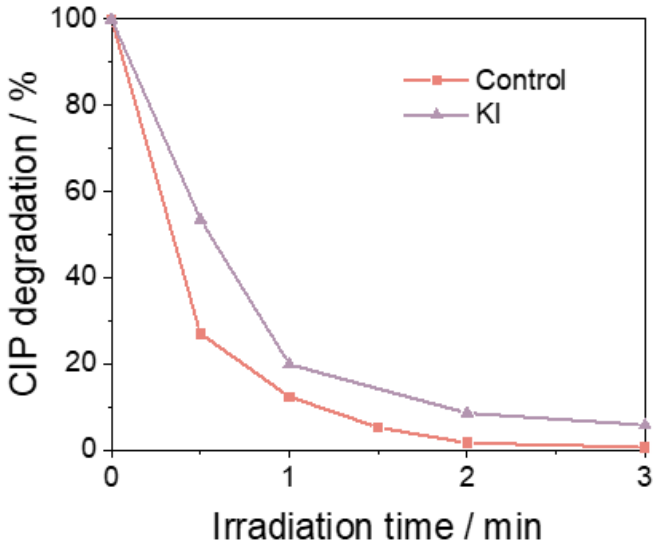

Figure S19. CIP degradation in the P/M-FeS_2 photo-Fenton system with and without KI addition as a h^+ trapping reagent.

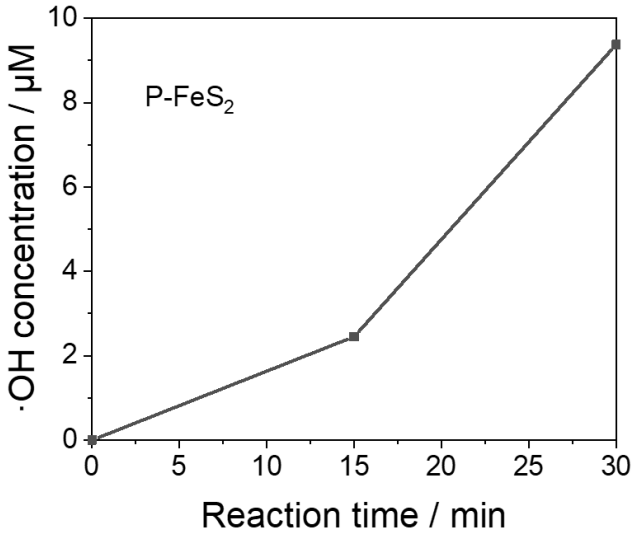

Figure S20. •OH radicals generated in the P-FeS_2 and H_2O system under Xe lamp with Ar purging.

The •OH radicals is measured as follows: 10 mg P-FeS_2 is added into a round-bottomed flask containing 50 ml H_2O, and then 1 mM coumarin solution is added therein. The flask is lined with the Schlenk-line. The system is evacuated and filled with Ar for 3 times and then the reaction starts. The concentration of •OH radicals is determined by fluorescence method as reported with the excitation wavelength of 350 nm and emission wavelength of 450 nm.[14] 7-hydroxycoumarin is measured to determine the •OH concentration with a production yield of 6.1% from coumarin and •OH.

Table S4. Fe:S ratios in P-FeS_2 and P-FeS_2 before and after the reaction.

	P-FeS_2			**M-FeS_2**		
Content/at%	Fe	S	Fe:S	Fe	S	Fe:S
Before reaction	1.73	47.7	1:27.6	3.40	35.7	1:10.5
After reaction	1.74	28.9	1:16.6	0.67	30.5	1:45.5

Table S5. The number of Fe and S atoms in surface model for P-FeS_2 and M-FeS_2.

	Fe	**S**	**Fe:S**
P-FeS_2	21	64	1:3
M-FeS_2	16	32	1:2

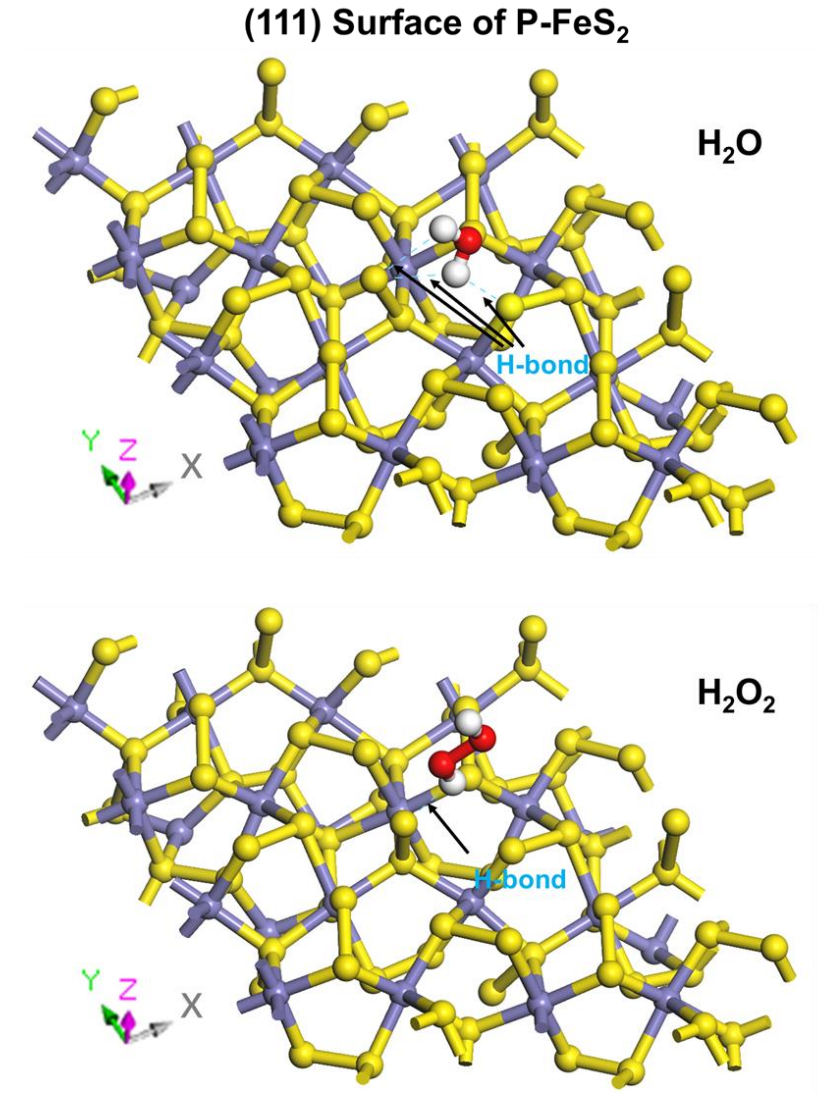

Figure S21. H-bonds formation between H_2O (top) and H_2O_2 (bottom) and the (111) surface of P-FeS_2.

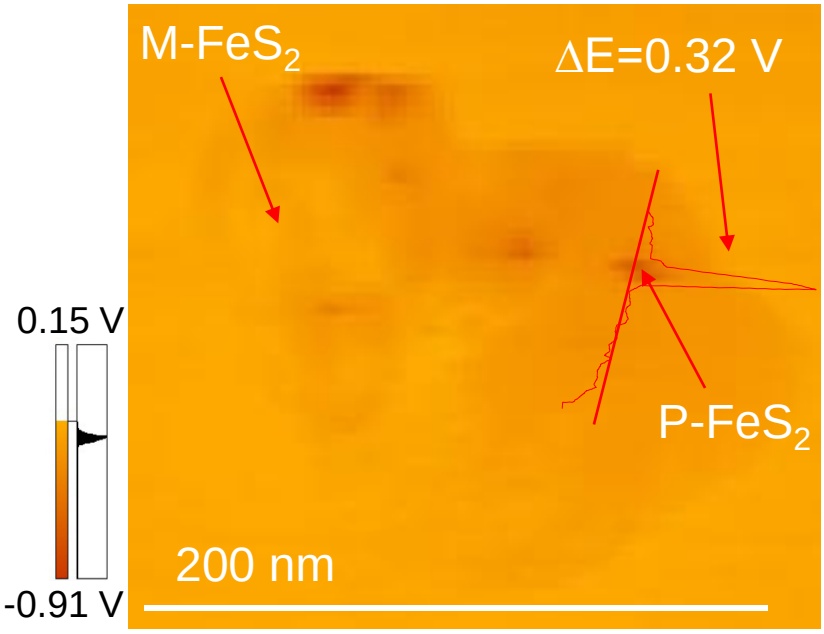

Figure S22. Surface potential difference between the pyrite and marcasite region in P/M-FeS_2 measure by KPFM.

References

1. Clark, S.J.; Segall, M.D.; Pickard, C.J.; Hasnip, P.J.; Probert, M.I.; Refson, K.; Payne, M.C. First principles methods using CASTEP. *Z. FÜR Krist. Cryst. Mater.* **2005**, *220*, 567–570. https://doi.org/10.1524/zkri.220.5.567.65075.
2. Liu, Y.; Wu, M.; Ren, L.; Wang, C.; Li, Z.; Ling, L.; Guo, Y.J. Heterogeneous photo-Fenton catalytic oxidation of ciprofloxacin using $LaFeO_3$/Diatomite composite photocatalysts under visible light. *ChemistrySelect* **2020**, *5*, 14792–14799. https://doi.org/10.1002/slct.202004136 .
3. Harini, G.; Okla, M.K.; Alaraidh, I.A.; Mohebaldin, A.; Al-Ghamdi, A.A.; Abdel-Maksoud, M.A.; Abdelaziz, R.F.; Raju, L.L.; Thomas, A.M.; Khan, S.S.J.C. Sunlit expeditious visible light-mediated photo-Fenton degradation of ciprofloxacin by exfoliation of $NiCo_2O_4$ and $Zn_{0\cdot3}Fe_{2\cdot7}O_4$ over g-C_3N_4 matrix: A brief insight on degradation mechanism, degraded product toxicity, and genotoxic evaluation in *Allium cepa*. *Chemosphere* **2022**, *303*, 134963. https://doi.org/10.1016/j.chemosphere.2022.134963.
4. Yang, C.P.; Hu, C.Y.; Jiang, Z.W.; Xiao, S.Y.; Wang, X.Y.; Huang, C.Z.; Li, Y.F.; Zhen, S.J.; Science, I. Facile synthesis of porphyrin-MOFs with high photo-Fenton activity to efficiently degrade ciprofloxacin. *J. Colloid Interface Sci.* **2022**, *622*, 690–699. https://doi.org/10.1016/j.jcis.2022.04.104.
5. Li, K.; Zhang, X.; Huang, X.; Li, X.; Chang, Q.; Deng, S.; Zhu, G.J. MOF-on-MOF-derived FeZr bimetal oxides supported on hierarchically porous carbonized wood to promote photo-Fenton degradation of ciprofloxacin. *J. Water Process Eng.* **2024**, *63*, 105442. https://doi.org/10.1016/j.jcis.2022.04.104.
6. Liu, L.; Dong, W.; Niu, M.; Liu, X.; Xue, J.; Tang, A.J. Fabrication of a confined pyrite cinder-based photo-Fenton catalyst and its degradation performance for ciprofloxacin. *J. Mol. Liq.* **2022**, *360*, 119489. https://doi.org/10.1016/j.molliq.2022.119489.
7. Xu, J.; Hu, D.; Wang, Y.; Zhang, Z.J.; Research, P. α-(Fe, Cu) OOH/RGO nanocomposites for heterogeneous photo-Fenton-like degradation of ciprofloxacin under visible light irradiation. *Environ. Sci. Pollut. Res.* **2022**, *29*, 78874–78886. https://doi.org/10.1007/s11356-022-21245-3.
8. Pan, Y.; Hu, X.; Shen, D.; Li, Z.; Chen, R.; Li, Y.; Lu, J.; Bao, M.J.; technology, p., Facile construction of Z-scheme Fe-MOF@ BiOBr/M− CN heterojunction for efficient degradation of ciprofloxacin. *Sep. Purif. Technol.* **2022**, *295*, 121216. https://doi.org/10.1016/j.seppur.2022.121216.
9. Wang, D.; Li, H.; Han, Q.; Jiang, W.; Liu, C.; Che, G.J.; Solids, C. Optimized design of $BiVO_4$/NH_2-MIL-53(Fe) heterostructure for enhanced photocatalytic degradation of methylene blue and ciprofloxacin under visible light. *J. Phys. Chem. Solids* **2021**, *154*, 110027. https://doi.org/10.1016/j.jpcs.2021.110027.
10. Chen, Y.; Zhang, X.; Wang, L.; Cheng, X.; Shang, Q.J. Rapid removal of phenol/antibiotics in water by Fe-(8-hydroxyquinoline-7-carboxylic)/TiO_2 flower composite: Adsorption combined with photocatalysis. *Chem. Eng. J.* **2020**, *402*, 126260. https://doi.org/10.1016/j.cej.2020.126260.
11. Meng, D.; Lei, Y.; Pang, M.; Qiu, J.; Fan, C.; Feng, Y.; Wang, D.J. Construction of highly active Fe/N-CQDs/MCN1 photocatalytic self-Fenton system for degradation of ciprofloxacin. *J. Environ. Chem. Eng.* **2023**, *11*, 110318. https://doi.org/10.1016/j.jece.2023.110318.
12. Zhang, X.; Lin, B.; Li, X.; Wang, X.; Huang, K.; Chen, Z.J. MOF-derived magnetically recoverable Z-scheme $ZnFe_2O_4$/Fe_2O_3 perforated nanotube for efficient photocatalytic ciprofloxacin removal. *Chem. Eng. J.* **2022**, *430*, 132728. https://doi.org/10.1016/j.cej.2021.132728.
13. He, W.; Jia, H.; Li, Z.; Miao, C.-q.; Lu, R.; Zhang, S.; Zhang, Z.J. Magnetic recyclable g-C_3N_4/Fe_3O_4@MIL-100(Fe) ternary catalyst for photo-Fenton degradation of ciprofloxacin. *J. Environ. Chem. Eng.* **2022**, *10*, 108698. https://doi.org/10.1016/j.jece.2022.108698.
14. Zhang, J.; Nosaka, Y. Quantitative detection of OH radicals for investigating the reaction mechanism of various visible-light TiO_2 photocatalysts in aqueous suspension. *J. Phys. Chem. C* **2013**, *117*, 1383–1391. https://doi.org/10.1021/jp3105166.